Supplementary Information for

Unlocking the performance of ternary metal (hydro)oxide amorphous catalysts via data-driven active-site engineering

Doudou Zhang, Haobo Li, Haijiao Lu, Zongyou Yin, Zelio Fusco, Asim Riaz, Karsten Reuter, Kylie Catchpole, and Siva Karuturi**

Dr. Doudou Zhang, Dr. Zelio Fusco, Asim Riaz, Prof. Kylie Catchpole and A/P. Siva Karuturi
School of Engineering, College of Engineering, Computing and Cybernetics, The Australian National University Canberra, ACT 2601, Australia

Dr. Haobo Li
School of Chemical Engineering, The University of Adelaide, Adelaide, South Australia 5005, Australia

Dr. Haijiao Lu, A/P Zongyou Yin
Research School of Chemistry, The Australian National University, Canberra, Australian Capital Territory 2601, Australia

Dr. Haobo Li and Prof. Karsten Reuter
Fritz-Haber-Institut der Max-Planck-Gesellschaft, 14195 Berlin, Germany
* Correspondence to E–mail: siva.karuturi@anu.edu.au ; haobo.li@adelaide.edu.au

Key words: multi-metallic, amorphous catalyst, machine-learning, OER performance, stability

Experimental Methods

Chemicals. All chemicals were of analytical grade and were used as-purchased without further purification. Aqueous solutions were prepared using high purity water produced from a Millipore Milli-Q Purification system (resistivity >18 MΩ cm). Nickel foam (purchased from Xiamen Tmax Battery Equipments Limited Co., Ltd with 80-100 pore density, 1.6mm thickness, 20mm*30mm) was cleaned by sequential ultrasonication in acetone, ethanol, and deionized water for 30 min each to clean the surface for further use. All the glassware was cleaned using the aqua regia solution, followed by rinsing with DI water.

$NiFe(OH)_x$ catalyst fabrication. For the preparation of corrosive solution, a certain amount of nickel salts (e.g., $Ni(NO_3)_2{\cdot}6H_2O$ (2 mM, 0.293g); $Fe(NO_3)_2{\cdot}6H_2O$(2 mM, 0.808g)) was added into 50 mL deionized water to make a transparent Ni^{2+}, Fe^{2+} solution in a petri dish. Then the nickel foam substrates were immersed in the corrosive solution at room temperature (～25 °C) for 48 h. The concentration of the corrosive solution was also varied to 6mM, 7.5 mM and 10 mM.

$Ni_xFe_yCo_z(OH)_m$ catalyst fabrication. For the preparation of $Ni_xFe_yCo_z(OH)_m$ catalyst using the same concentration corrosive solution, a certain amount of nickel salts (e.g., $Ni(NO_3)_2{\cdot}6H_2O$ (2 mM, 0.293 g); $Fe(NO_3)_2{\cdot}6H_2O$(2 mM, 0.808 g)), with additional $Co(NO_3)_2$ (2 mM, 0.293 g)) was added into 50 mL deionized water to make a transparent Ni^{2+}, Fe^{2+}, and Co^{2+} solution in a petri dish.Then the nickel foam substrates were immersed in the corrosive solution at room temperature (～25 °C) for 48 h. The concentration of the corrosive solution was also varied to 6mM, 7.5 mM and 10 mM.

For comparison, we attempted to create the corrosive solutions using only cations, such as Ni^{2+}, Fe^{2+}, Co^{2+} and higher valence states, such as Fe^{3+} or different anions (SO_4^{2-}) in lieu of NO_3^-. Correspondingly, the corrosion reactions resulted in the formation of only Ni containing, Fe-containing, or NiFe-containing, NiFeCo-containing or even no thin films on the nickel foam substrates.

Structural and morphological characterization. SEM characterizations to obtain surface images of the synthesized samples were carried out using a Scanning Electron Microscopy Cathodoluminescence (SEM-CL) system. The crystallinity of the samples was examined by XRD measurements on a Bruker system (D Phaser, USA) equipped with Cu Kα radiation with an average wavelength of 1.54059 Å. The typical scan range (2θ) was 10^{o} to 80^{o} collected with a step size of 0.039^{o} s^{-1}. The TEM and HRTEM images were obtained on a JEF2100 (JEOL company) with an acceleration voltage of 200 kV. XPS measurements were performed with a Thermo ESCALAB250i. The high-resolution measurements were conducted with 500 μm spot size and a pass energy of 20 eV. To ensure the consistency of the results, the scan was performed at 4 different spots. The binding energies reported in this study were calibrated to adventitious hydrocarbon at 284.8 eV.

Electrochemical measurements. Current density vs. potential curves were recorded with a commercial potentiostat (CHI760D electrochemical workstation) in a standard three-electrode configuration, with a Luggin capillary joining the reference electrode (RE) to the working electrode (WE) compartment. A graphite rod and Ag/AgCl were used as the counter electrode and RE, respectively. The counter electrode was cleaned by sequential ultrasonication in acetone, ethanol, and deionized water for 30 min each to clean the surface for use. The measured current values were converted to current density values by dividing them by the geometric areas of the anodes. Electrochemical measurements were carried out in 1.0 M KOH aqueous solution. The applied potential was swept from 1 to 1.7 V vs. RHE at a scanning rate of 5 mV s^{-1}. All the electrochemical experiments were carried out at room temperature (25°C). The overpotential values for different electrodes were collected at steady-state currents of 10 mA cm^{-2} from chronopotentiometry measurements.

The faradaic efficiency of $Ni_xFe_yCo_z(OH)_m$ catalyst was measured in an H-type electrochemical cell with a Sustainion 37 membrane separator (purchased from Dioxide

materials Co., Ltd). Prior to its utilization in the test, we wetted it by DI water, followed by its activation in the 1M KOH solution over night. Gas samples were collected using an airtight syringe at 15 min intervals and injected into a gas chromatograph (SHIMADZU GC-2030 system, TCD, Argon carrier) for the detection of the generated oxygen. Before measurement, the reaction system was thoroughly degassed with ultrapure nitrogen to expel the entrapped air. Then, a constant current density of 10 $mAcm^{-2}$ was applied to the electrode and the concentration of oxygen was analyzed. Calibrations were carried out using a similar setup but with two cleaned Pt foils as working and counter electrodes. The EIS measurement of zero-gap cells was carried out at a potential of 1.6 V and an AC frequency ranging from 100 kHz to 100 mHz.

Computational details

Spin-polarized DFT calculations were performed with the plane-wave basis, pseudopotential package Quantum ESPRESSO (QE)[1, 2] using the van der Waals-corrected BEEF-vdW exchange correlation functional[3]. Surface structures were modelled as fully optimized symmetric slabs separated by a vacuum region of 20 Å. The layered double (hydro)oxide (LDH) in β-phase was calculated with a (3x3) unit cell (**Fig. S9**). Comprehensive test calculations of model layers for all the intermediates (*OH, *O, *OOH, $*O_2$) have been performed. To correspond to the experimental value of thickness of ~10Å, 1-3 layers of NiO_2 and 1-2 layers of $Ni(OH)_2$ were considered. As shown in **Table S2**, variations in the number of model layers have a minimal impact on the adsorption energies of all intermediates for NiO_2, with differences within 0.1 eV. While for $Ni(OH)_2$, the effect is slightly more pronounced, around 0.2 eV, it still does not significantly alter the methodology or the primary conclusions of the study. Therefore, only the single-layer structure was used for further calculations to streamline high-throughput computations without compromising accuracy. The three Ni atoms and one O(H) on the corner (shown as transparent) were fixed and the other atoms fully

optimized. This makes 6 metal atoms (marked as 1-6) and their neighbouring O (and H) atoms relaxed. The Hubbard U correction was applied to d-orbitals of Fe, Co, Ni with the values of 2.56, 3.50 and 5.20 eV[4], respectively. The effects of spin-polarization and U on the adsorption energy were tested as shown in **Table S3**. The plane-wave cut-off was set to 800 eV and the k-grid to (3x3x1). Test calculations with higher cut-offs and k-point grids indicated the adsorption energies were converged within 15 meV and 0.4 meV, respectively (**Table S4**). The bulk (hydro)oxide was calculated with a (1x1x1) unit-cell and a (12x12x12) *k*-grid. As the optimized lattice constant for Fe, Co, Ni (hydro)oxide is within a difference of 2.7% to $Ni(OH)_2$ and 0.15% to NiO_2 (**Table S5**), the lattice constant was then set to the value of Ni (hydro)oxide for the further calculations. The gas-phase molecules (H_2 and H_2O) were calculated for electronic energies and vibrational frequencies separately in each supercell with a side length of 10 Å. The adsorption energies were calculated by: $E_{ad} = E_{adsorbate/surface} - E_{surface} - \mu_{adsorbate}$ and the adsorption free energies were then calculated with vibrational free energy corrections: $G_{ad} = E_{ad} + ZPE + \int C_p dT - TS + \Delta G_{sol}$ (**Table S6**). Solvation effects corrections (ΔG_{sol}) were calculated for the hydrogen-containing groups (*OH, *OOH) within an implicit model approach using the Environ[5, 6] module provided with QE (**Table S7**). The magnetic moment attributed to Fe, Co or Ni atoms were calculated by the "magn" tag in "Magnetic moment per site" from the QE output file.

Machine learning

The well-established symbolic regression algorithm SISSO [7, 8] has been used to identify the best sparse solution out of an immense feature space spanned by various nonlinear combinations of primary features. The operators are applied iteratively to the generated feature spaces, with the number of iterations performed, *N,* being a hyperparameter of the method (denoted the rung, Φ_N). An increase of *N* leads to a rapidly growing size of the total feature

space, which improves the accuracy while increasing the amount of calculation. The SISSO training result is the operation between primary features with fitting coefficients as descriptors to represent the adsorption free energies (G_{ad}).

As shown in **Fig. S14**, two equations were formulated to capture the impact of the active site structure on adsorption energy, with the intention of accounting for the influence of each atom surrounding the adsorption site. The six neighbouring atoms are categorized into the first shell (atoms 2, 4, 6) and the second shell (atoms 1, 3, 5). Within the first shell, all three atoms have direct interactions with the adsorbed species. Consequently, the average value of these three atoms is utilized to calculate the indicative effect of the first shell on adsorption energy. The three atoms within the second shell do not directly interact with the adsorbed species but exert an influence on the first-shell atoms. For instance, atom 1 affects atoms 2 and 6, and thus the representation $(f_2*f_6)/f_1$ is employed. In this way, the structure of each unique adsorption site are well characterized through the chosen formulas.

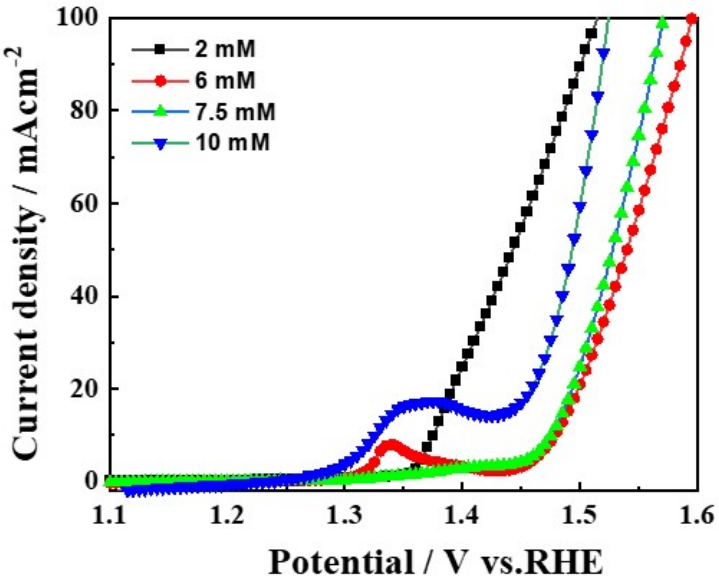

Fig. S1. OER performance of different $Ni_xFe_yCo_z(OH)_m$ electrodes. Polarization curves obtained in 1 M KOH for various $Ni_xFe_yCo_z(OH)_m$ electrodes fabricated using precursor concentrations of 2 mM, 6 mM, 7.5 mM, and 10 mM.

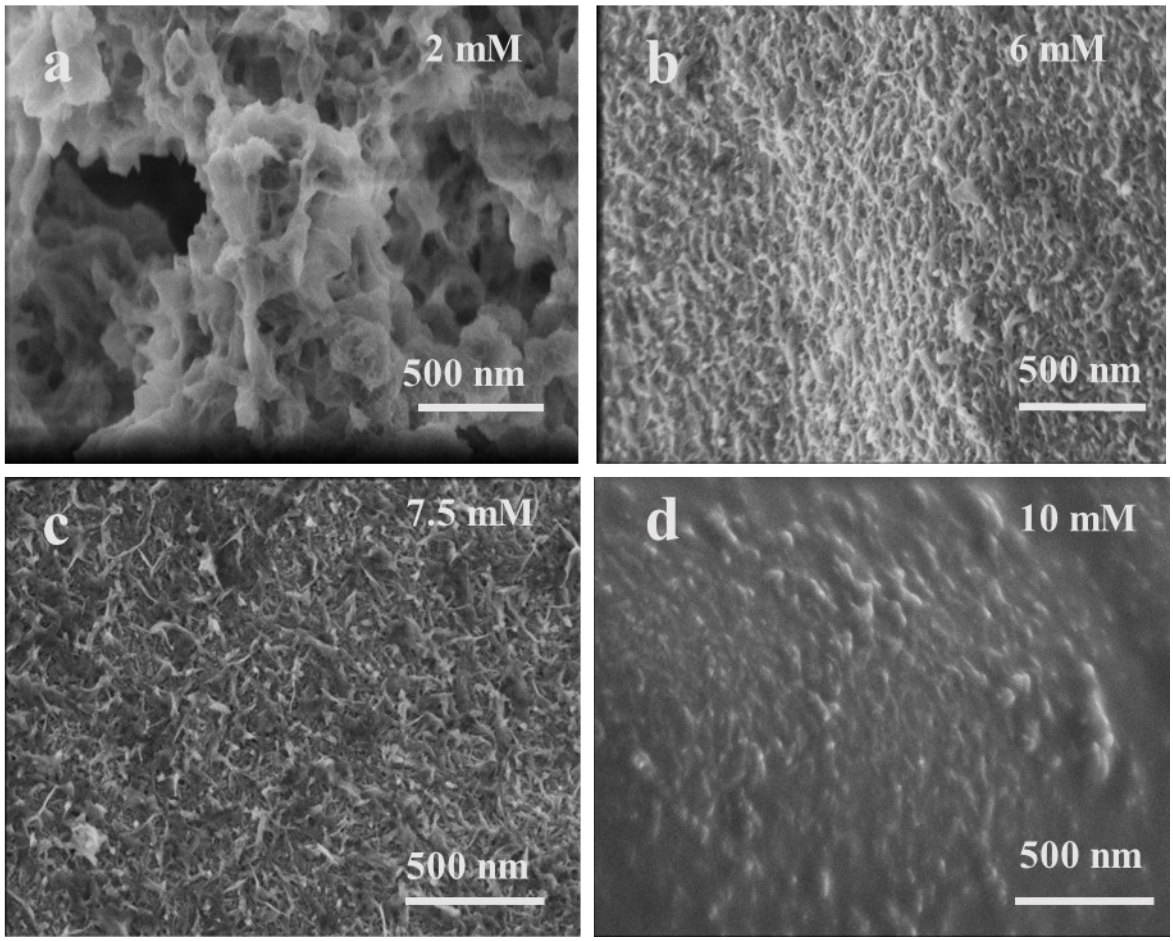

Fig. S2. SEM images of different $Ni_xFe_yCo_z(OH)_m$ electrodes. Scanning electron microscopy images of $Ni_xFe_yCo_z(OH)_m$ electrodes fabricated using different precursor concentrations of 2 mM, 6 mM, 7.5 mM, and 10 mM.

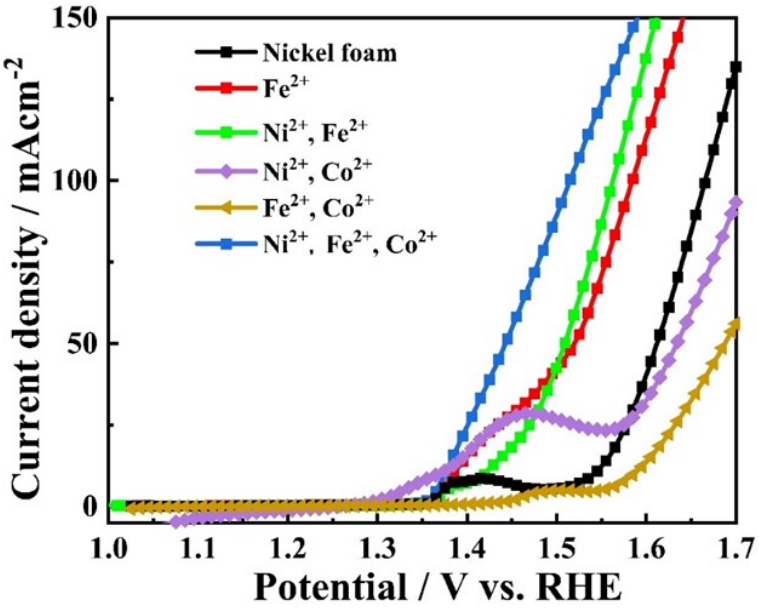

Fig. S3. OER performance of mono-, bi-, and tri-metallic electrodes. Polarization curves were obtained in 1 M KOH for electrodes fabricated using the following precursors: Fe^{2+} precursor, bi-metallic precursors of Ni^{2+} and Fe^{2+}, Ni^{2+} and Co^{2+}, Fe^{2+} and Co^{2+}, and tri-metallic precursors of Ni^{2+}, Fe^{2+}, and Co^{2+}.

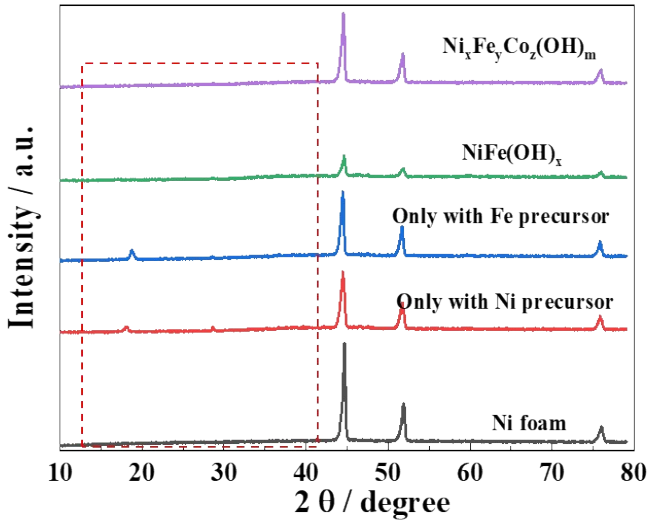

Fig. S4. Structure characterization. XRD patterns of the different electrodes fabricated using Ni^{2+} precursor, Fe^{2+} precursor, a combination of Ni^{2+} and Fe^{2+} precursors, and a combination of Ni^{2+}, Fe^{2+}, and Co^{2+} precursors.

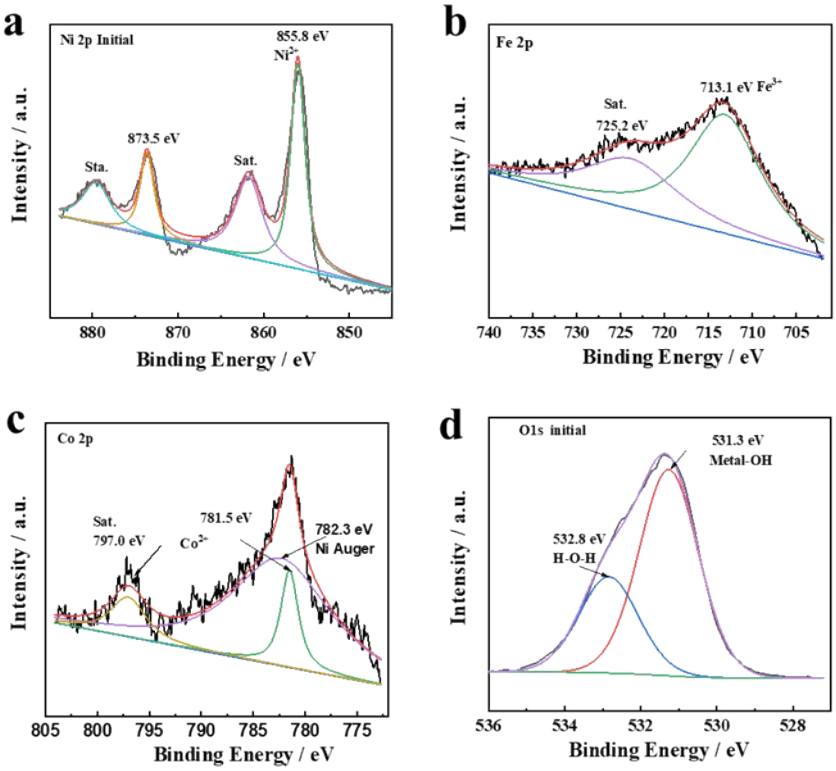

Fig. S5. X-ray photoelectron spectroscopy spectra. (a) Ni 2p, (b) Fe 2p, (c) Co 2p and (d) O1s of ternary $Ni_xFe_yCo_z(OH)_m$ (hydro)oxides.

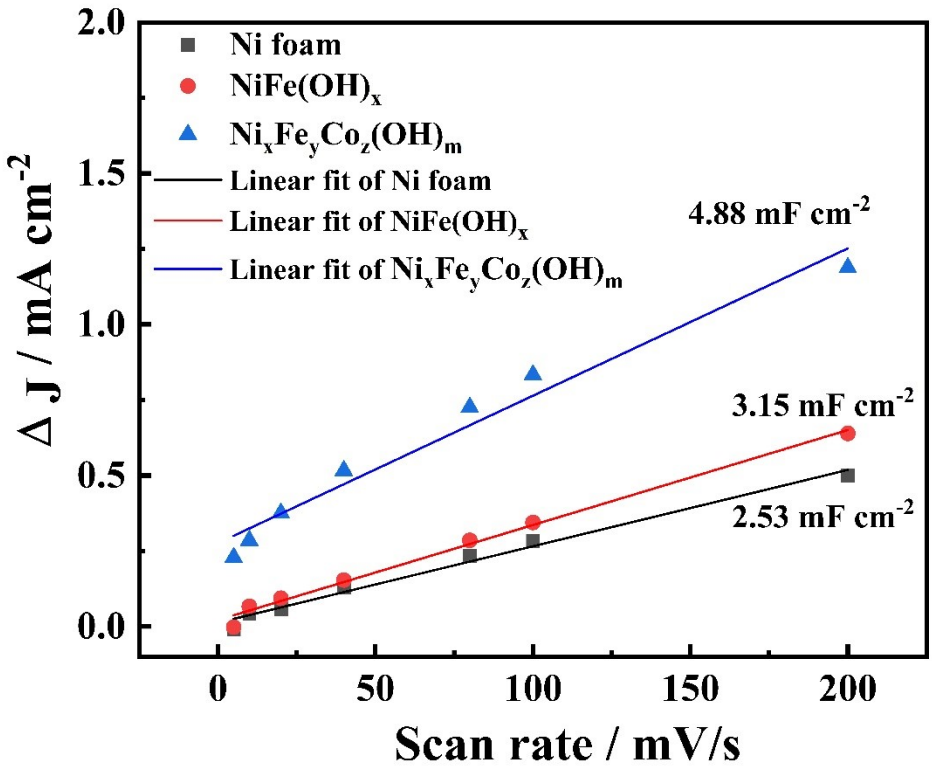

Fig. S6. Electrochemical surface area evaluation. The linear fittings of the capacitive currents of Ni foam, NiFe(OH)x and $Ni_xFe_yCo_z(OH)_m$ electrodes as a function of scan rate.

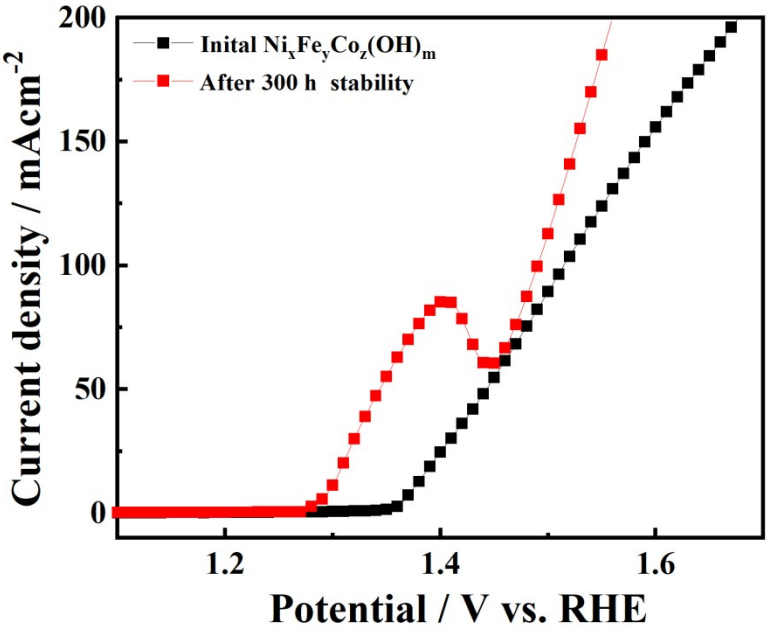

Fig. S7. Performance of $Ni_xFe_yCo_z(OH)_m$ electrodes before and after stability test. Comparison LSV curves of $Ni_xFe_yCo_z(OH)_m$ electrodes before and after 300 hours operation.

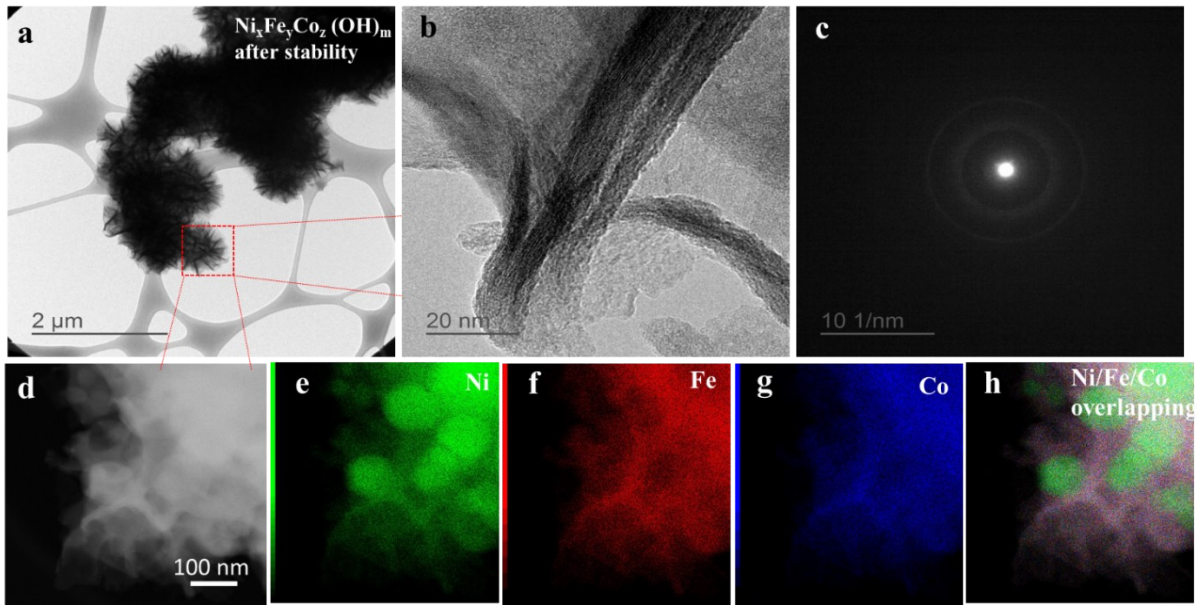

Fig. S8. Structure characterization of $Ni_xFe_yCo_z(OH)_m$ after stability test. (a) Transmission electron microscopy (TEM) image and (b) the corresponding high resolution transmission electron microscopy (HRTEM) image and (c) selected-area electron diffraction (SAED) patterns collected from the square marked in **Fig. S8a**. (d-h) TEM images from the selected area and the corresponding elemental mappings of ternary $Ni_xFe_yCo_z(OH)_m$ alloy hydroxyl after 300 hours stability test.

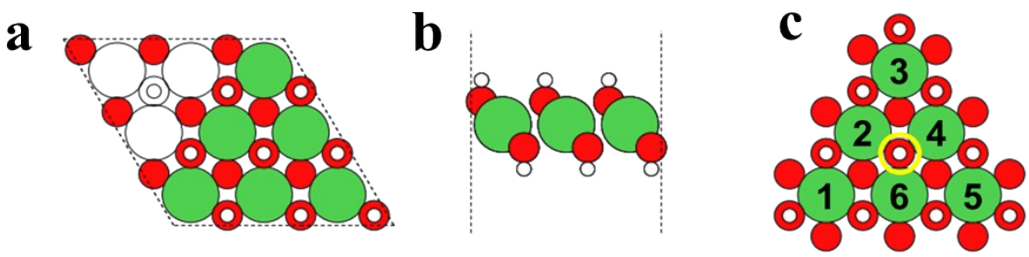

Fig. S9. (a-b) Top (a) and side (b) view of a unit cell of $Ni(OH)_2$. The atoms not included in the active-site structure are shown transparent. Ni: Green spheres; O: red spheres; H: white spheres. (c) Active-site structure consisted of 6 metal (Fe, Co, Ni) atoms with neighbouring O (and H) atoms. The active site is marked by the yellow circle.

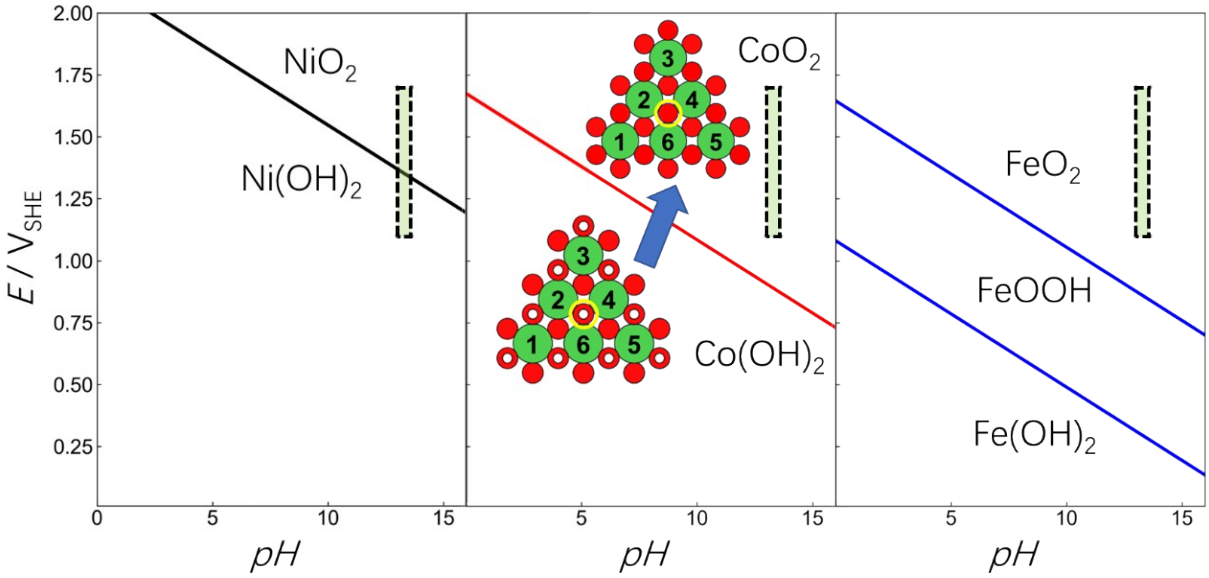

Fig. S10. Surface Pourbaix diagram of Fe, Co, Ni (hydro)oxide. The experimental condition lies inside the zone marked by dashes.

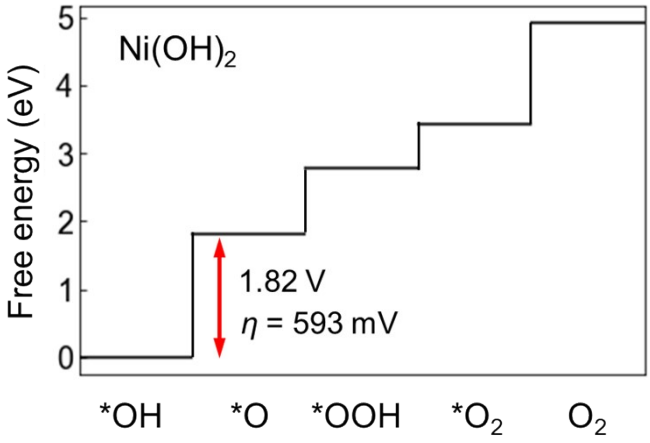

Fig. S11. Reaction free-energy diagrams for OER on $Ni(OH)_2$.

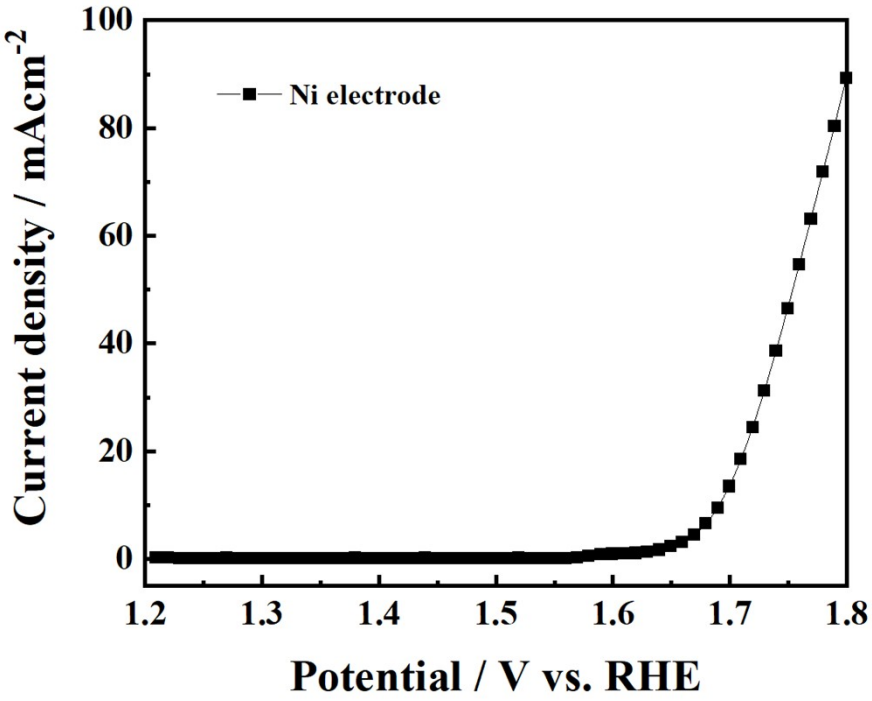

Fig. S12. Polarization curve of a planar Ni planar electrode in 1.0 M KOH.

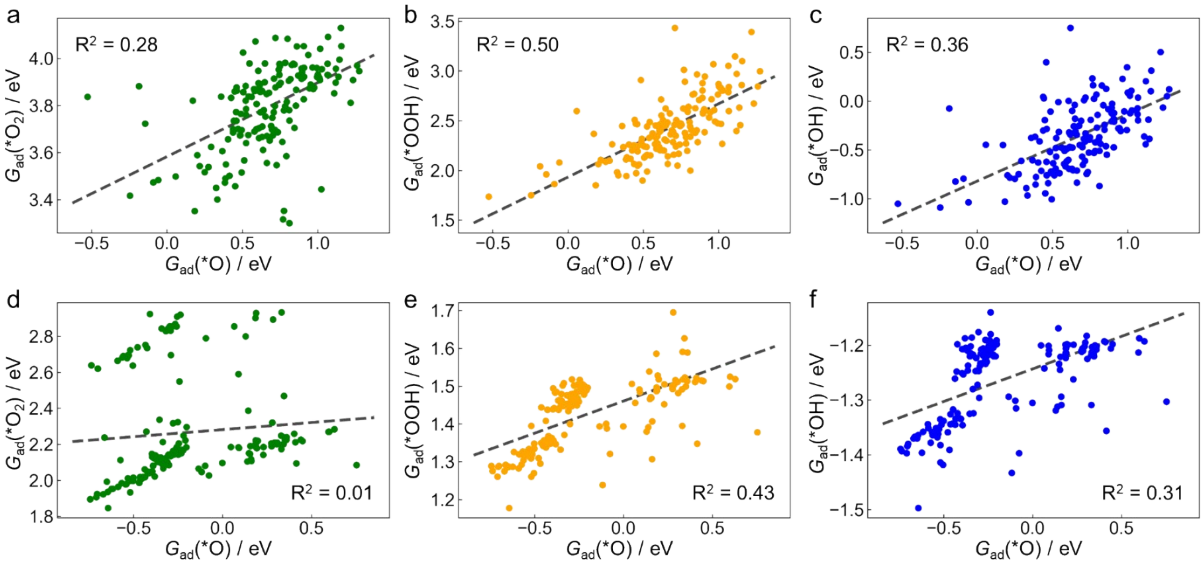

Fig. S13. Relationship between the adsorption free energies (G_{ad}) of the 3 intermediate adsorbates (*OH, *OOH, *O_2) with the adsorbate *O on MO_2 (a-c) and $M(OH)_2$ (d-f) active-sites. As a supplement to **Fig. 3a, d**. Gray dashed lines are linear fits to the data, with the R^2 coefficient explicitly provided.

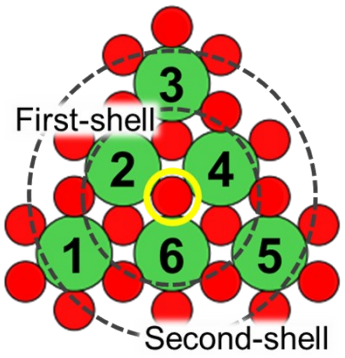

$$F\_1 = F\,(\text{First-shell}) = (f_2 + f_4 + f_6)/3$$

$$F\_2 = F\,(\text{Second-shell}) = (f_2{*}f_6/f_1 + f_2{*}f_4/f_3 + f_4{*}f_6/f_5)/3$$

Fig. S14. Scheme of the positions of first-shell and second-shell metal atoms around the active-site.

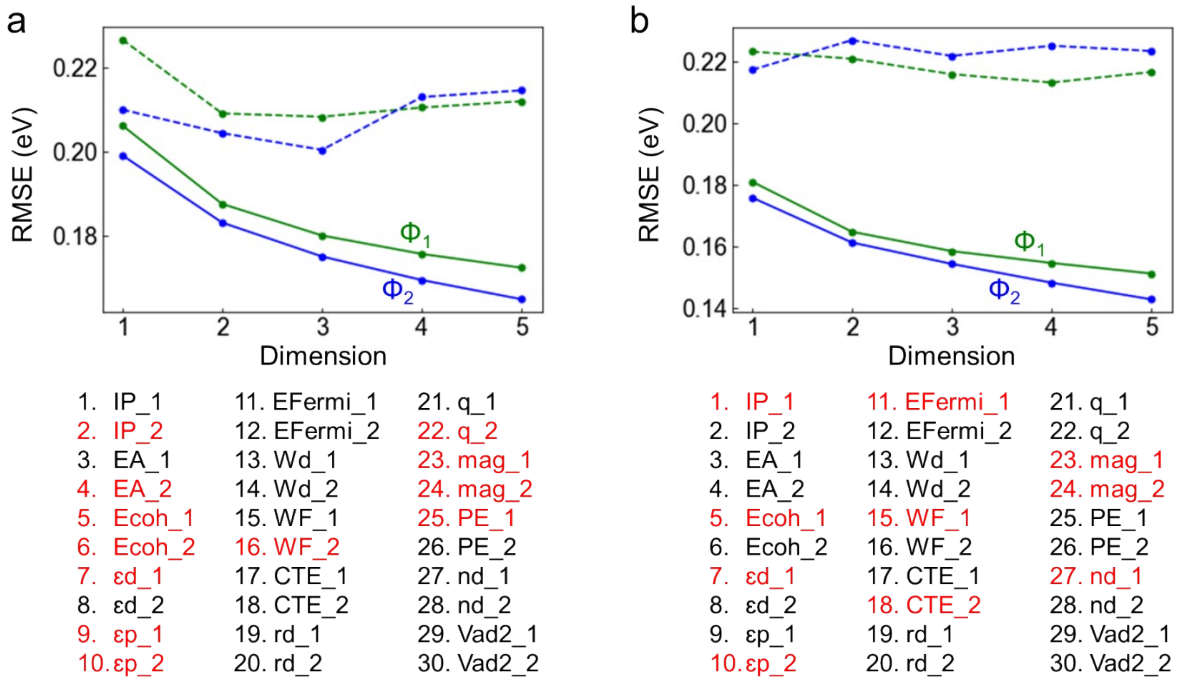

Fig. S15. RMSE for the multi-task training descriptors (solid line) and a 5-fold cross-validation (dashed line) in MO_2 (a) and $M(OH)_2$ (b). The features used are listed below the plots, where the features selected by SISSO are marked in red.

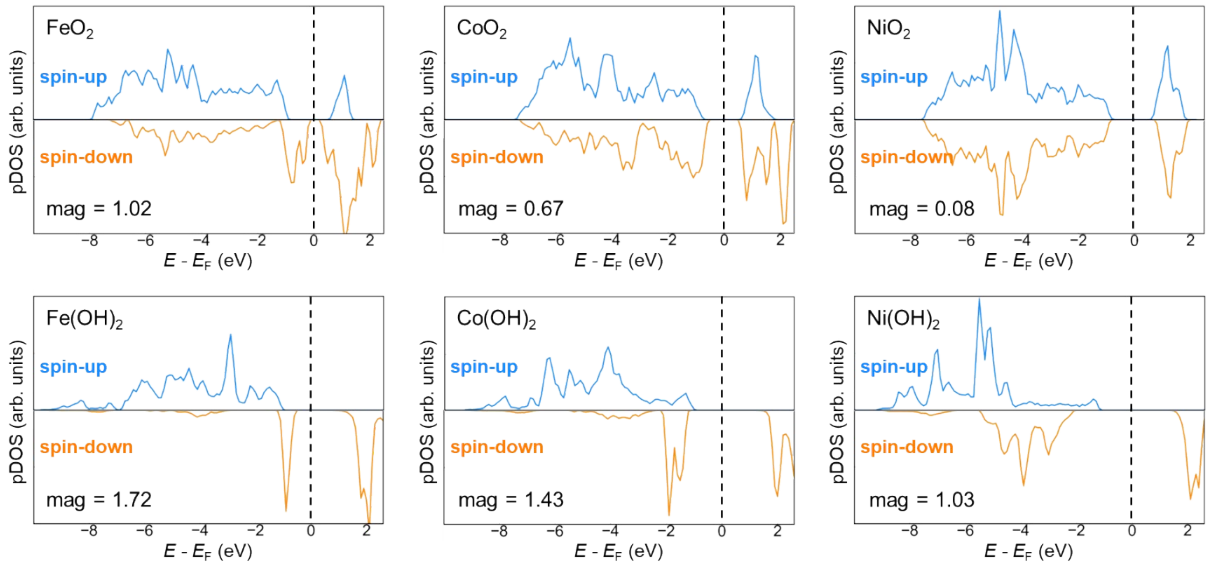

Fig. S16. Projected electronic density of states (pDOS) for Fe, Co, Ni *d* orbital of active site atoms on Fe, Co, Ni (hydro)oxide, respectively. The Fermi-level is used as zero reference. The calculated magnetic moments (mag) are indicated accordingly.

Table S1. Comparison of the reported OER performance of robust earth-abundant electrocatalysts in 1.0 M KOH on porous substrates

Catalyst	Substrate	Tafel slope (mV/decade)	Overpotential V vs. RHE at 10 mA cm^{-2}	Stability / h	Reference
$Ni_xFe_yCo_z(OH)_m$	Ni foam	50	146	300 / 12.5 days	Our work
NiFeS@OCC	Carbon cloth	75	220	48	J. Mater. Chem. A, 2021, 9, 24299-24307
Co_9S_8@NiFe-LDH-200	Ni foam	52.8	190	100	Journal of Colloid and Interface Science,2021, 604, 680-690
Ultrathin NiFeRh-LDH nanosheets	Ni foam	29	204	45	Applied Catalysis B: Environmental,2021,284, 119740
$Ni_{0.8}Fe_{0.2}$-AHNA	Ni foam	34.7	190	120	Energy Environ. Sci., 2020, 13, 86-95
NiFe/NiFe–OH core shell	Ni foam	41	222	24	Applied Catalysis B: Environmental,2020, 278, 119326
NF/$Co_{5.0}Mo_1P$	Ni foam	55	NA	24	ACS Appl. Energy Mater. 2020, 3, 8075-8085
P-V-NiFe LDH nanosheet array	Ni foam	56	NA	100	Applied Catalysis B: Environmental,2020,266,118627
Pt–NiFe-LDH	Ni foam	64	NA	20	Nano Energy,2020, 72, 104669
Ru-NiFe-P	Ni foam	66.1	NA	24	Applied Catalysis B: Environmental, 2020, 263, 118324
NiFe-BTC GNPs MOF	Carbon-fiber-paper	51	220	96	Energy Environ. Sci., 2020, 13, 3447-3458
Fe-NiMo-NH_3/H_2	Ni foam	28	192	25	Adv. Energy Mater,2020, 10, 2002285
Se-	Ni foam	33.9	155	73	Adv. Mater., 2018,

$(NiCo)S_x/(OH)_x$ Nanosheets					30(12): 1705538
FeCoNi-hybrid nanotube arrays	Ni foam	49.9	184	80	Nat. Commun., 2018, 9(1): 2452
Fe@NiFe LDH	Fe foam	48.3	269	100	Nat. Commun., 2018, 9(1): 2609
Ni-Fe-O mesoporous nanowire	Ni foam	39	244	60	Adv. Energy Mater., 2018, 8(5): 1701347
Ni/Fe (oxy)hydroxide nanorod arrays	Ni foam	41.5	150	44	Energy Environ. Sci., 2018, 11(10): 2858-2864
NiFe LDH/Cu nanowire arrays	Cu foam	27.8	199	48	Energy Environ. Sci.,2017, 10(8): 1820-1827
Ni-Fe-OH@Ni_3S_2	Ni foam	93	165	50	Adv. Mater., 2017, 29(22): 1700404
Core-Shell Ni-Co Nanowire	Carbon fiber	43.6	302	10	Adv. Energy Mater., 2017, 7(1): 1601492
Ni_3FeN-NPs	Ni foam	46	280	9	Adv. Energy Mater., 2016, 6(10): 1502585
NiFe LDH/CNTs	Carbon paper	31	300	1	J. Am. Chem. Soc.,2013, 135(23): 8452-8455
Ultrathin NiCo-MOF	Ni foam	42	189	11.1	Nature Energy, 2016, 1,1-9

Table S2. Adsorption energies (E_{ad}) (unit: eV) of all reaction intermediates (*OH, *O, *OOH, $*O_2$) on different layer numbers of NiO_2 and $Ni(OH)_2$. The test is calculated with spin-off and without *U* corrections. The experimental value of the thickness is about 10 Å.

NiO_2	Thickness (Å)	E_{ad}(*OH)	E_{ad}(*O)	E_{ad}(*OOH)	E_{ad}(*O_2)
1 Layer	1.90	-0.37	0.74	2.51	3.81
2 Layers	6.52	-0.39	0.77	2.49	3.79
3 Layers	11.14	-0.42	0.75	2.46	3.76
$Ni(OH)_2$	Thickness (Å)	E_{ad}(*OH)	E_{ad}(*O)	E_{ad}(*OOH)	E_{ad}(*O_2)
1 Layer	4.01	-0.05	0.44	2.78	2.77
2 Layers	8.67	-0.24	0.46	2.66	2.57

Table S3. Adsorption energies (E_{ad}) of *O on single-layered NiO_2 and $Ni(OH)_2$. A comparison of spin-on/off and w/o Hubbard *U* correction.

E_{ad}(*O) (eV)	spin-on +*U*	spin-off +*U*	spin-on	spin-off
NiO_2	1.05	0.83	0.74	0.74
$Ni(OH)_2$	0.58	0.97	0.17	0.44

Table S4. Adsorption energies (E_{ad}) of *O on single-layered $Ni(OH)_2$ using varying computational settings.

k-point grid	E_{ad}(*O) (eV)
3x3x1	**0.5849**
4x4x1	0.5847
5x5x1	0.5845
6x6x1	0.5845
Energy cutoff (eV)	E_{ad}(*O) (eV)
800	**0.5849**
1000	0.5697
1200	0.5704

Table S5. Optimized lattice constant of *β*-Fe, Co, Ni (hydro)oxide. There are minimal differences in lattice dimensions between the oxides and hydroxides of Fe, Co, and Ni elements in the a, b, and c directions. It indicates that Fe, Co, and Ni doping has an insignificantly small impact on lattice strain. The influence of bulk lattice on adsorption energy can thus be ignored.

Lattice constant (Å)	NiO_2	CoO_2	FeO_2
a	2.8348	2.8306	2.8382
b	2.8348	2.8306	2.8382
c	4.5299	4.4524	4.5242
Lattice constant (Å)	**$Ni(OH)_2$**	**$Co(OH)_2$**	**$Fe(OH)_2$**
a	3.2079	3.1622	3.1205
b	3.2079	3.1622	3.1205
c	4.6188	4.7728	4.5434

Table S6. Free energy corrections applied to the adsorbates.

Adsorbate	ZPE (eV)	$\int C_p dT$ (eV)	TS (eV)
***OH**	0.37	0.04	0.06
***O**	0.06	0.03	0.05
***OOH**	0.44	0.09	0.19
$*O_2$	0.14	0.07	0.14

Table S7. Solvation corrections applied to the adsorbates.

Adsorbate	ΔG_{sol} (eV)
***OH**	-0.0156
***OOH**	-0.0931

Table S8. Work function (WF) calculated on different layer numbers of NiO_2 and $Ni(OH)_2$. The results indicate that WF remains insensitive to the number of layers. Therefore, this work employs calculation data from a single layer.

NiO_2	WF (eV)

1 Layer	8.20
2 Layers	7.94
3 Layers	7.94
$Ni(OH)_2$	**WF (eV)**
1 Layer	2.93
2 Layers	2.69

Author contributions

D.Z., H. Li and S.K. conceived the work. D. Z. designed and carried out the experimental work, including synthesis and electrochemical and characterization measurements. Z. F. performed the AFM characterizations. H. Li. and K. R. performed the DFT and ML computations. H. Lu. A. Riaz and Z. Y. assisted with analysis of the findings. D. Z. and H. Li. wrote the manuscript. S.K, supervised the work. S.K., K. C. and K. R. edited the manuscript. All authors have reviewed and approved the final version of the manuscript.

References:

1. P. Giannozzi, S. Baroni, N. Bonini, M. Calandra, R. Car, C. Cavazzoni, D. Ceresoli, G. L. Chiarotti, M. Cococcioni and I. Dabo, *Journal of physics: Condensed matter*, 2009, **21**, 395502.

2. P. Giannozzi, O. Andreussi, T. Brumme, O. Bunau, M. B. Nardelli, M. Calandra, R. Car, C. Cavazzoni, D. Ceresoli and M. Cococcioni, *Journal of physics: Condensed matter*, 2017, **29**, 465901.
3. J. Wellendorff, K. T. Lundgaard, A. Møgelhøj, V. Petzold, D. D. Landis, J. K. Nørskov, T. Bligaard and K. W. Jacobsen, *Physical Review B*, 2012, **85**, 235149.
4. F. Dionigi, Z. Zeng, I. Sinev, T. Merzdorf, S. Deshpande, M. B. Lopez, S. Kunze, I. Zegkinoglou, H. Sarodnik and D. Fan, *Nature communications*, 2020, **11**, 1-10.
5. O. Andreussi, I. Dabo and N. Marzari, *The Journal of chemical physics*, 2012, **136**, 064102.
6. O. Andreussi, N. G. Hormann, F. Nattino, G. Fisicaro, S. Goedecker and N. Marzari, *Journal of chemical theory and computation*, 2019, **15**, 1996-2009.
7. R. Ouyang, S. Curtarolo, E. Ahmetcik, M. Scheffler and L. M. Ghiringhelli, *Physical Review Materials*, 2018, **2**, 083802.
8. R. Ouyang, E. Ahmetcik, C. Carbogno, M. Scheffler and L. M. Ghiringhelli, *Journal of Physics: Materials*, 2019, **2**, 024002.